Available online at www.sciencedirect.com

ScienceDirect

Ceramics International 40 (2014) 619–627

CERAMICS INTERNATIONAL

www.elsevier.com/locate/ceramint

Thermal shock resistance of two micro-structured alumina obtained by natural sintering and SPS

H. Belghalem[a,b], M. Hamidouche[b,c,*], L. Gremillard[d], G. Bonnefont[d], G. Fantozzi[d]

[a]Département de Génie Mécanique, Université Cheikh Larbi Tébessi, 12002 Tébessa, Algérie
[b]Unité de Recherche Matériaux Emergents, Université de Sétif 1, 19000, Algérie
[c]Laboratoire des Matériaux Non Métalliques, Institut d'Optique et Mécanique de, Précision, Université Sétif 1, 19000, Algérie
[d]Université de Lyon, INSA-Lyon, MATEIS CNRS-UMR 5510, 69621 Villeurbanne, France

Received 26 December 2012; received in revised form 29 May 2013; accepted 12 June 2013
Available online 1 July 2013

Abstract

In the present work, the indentation air quenching technique was used to evaluate thermal shock behavior of a micro-structured alumina obtained with different sintering techniques (Spark Plasma Sintering and natural sintering) and conditions (varying dwell time, dwell temperature and pressure). The main objective is to evaluate the effect of the sintering technique on the thermal shock properties, by comparing the mechanical and thermal shock properties between samples prepared by natural sintering and SPS. Another objective is to determine how the grains size and porosity affect the initiation and growth of cracks in samples submitted to thermal shocks of different amplitudes.

Keywords: C. Thermal shock resistance; Alumina; Microstructure; Sintering SPS

1. Introduction

The evolution of powders towards nanometric sizes plays a role in ceramics engineering to improve their performances, for instance their chemical inertness, hardness, and resistance to impact. Different industries use ceramics nanopowders in different areas such as electronics, energy, medical, environment and nanocomposites structure [1–4]. However, a difficulty of developing the use of these nanopowders comes from their tendency to agglomerate, resulting in low green density and subsequent grain growth during sintering.

During sintering, competition exists between particles coarsening and densification mechanisms that, respectively, lead either to porous structure with large grains, or to dense specimens followed by grain growth. Thus the use of new or improved sintering techniques is inevitable to increase the density and limit the growth.

Hot-pressing or sintering under pressure can reduce the sintering temperature. In this case, the driving force for sintering is increased and higher density can usually be obtained at a low sintering temperature. Hot pressing is particularly advantageous if a fine grain size is desired in a sintered ceramic, because less grain growth occurs at lower sintering temperature [5]. Spark Plasma Sintering (SPS) is similar to Hot Pressing Sintering in vacuum to the extent that graphite dies are used to apply a unidirectional pressure to the green body, while the specimen is heated to the sintering temperature using electric current pulses [6,7]. Rapid heating (some hundreds °C/min) is the characteristics for the SPS technique, and may help retain the advantage of the high specific surface area of nano-powders at high temperatures. Very short holding times are possible to obtain fully dense samples. The aim of SPS system is to minimize grain growth in order to prepare dense nanostructured materials [8–11].

A thermal shock occurs when a body is suddenly placed in contact with an environment that has a different temperature.

*Corresponding author at: Unité de Recherche Matériaux Émergents, Université Sétif 1, 19000, Algérie. Tel.: +213 36611704.
E-mail addresses: mhamidouche@univ-setif.dz, mhamidouche@yahoo.fr (M. Hamidouche).

0272-8842/$ - see front matter © 2013 Elsevier Ltd and Techna Group S.r.l. All rights reserved.
http://dx.doi.org/10.1016/j.ceramint.2013.06.045

The descending thermal shock is dangerous for brittle materials such as ceramics because it generates tensile stresses on the rapidly cooled surface. These stresses may be sufficient to activate pre-existing micro-cracks and may lead to material damage or fracture [12]. The shock intensity is related to the temperature difference level between the initial body temperature and that of the environment, and to the conditions in which the shock is applied, through the Biot number.

The amplitude of the critical temperature difference is related to the initial state, the geometry and the dimensions of the tested material [13]. The reliability of these materials is determined by two important factors: the fracture strength and the Weibull modulus. When strength tests are carried out on a set of similarly prepared samples, variability on the obtained strength values is observed [14]. The strength depends on the material structure and surface quality reflecting the size and the density distribution of the defects initiating fracture. These defects exert a great influence on the fracture characteristics [15]. In addition, the lower thermal conductivity of the structural ceramics at high temperature increases the Biot number. As consequence, the induced thermal stresses become more important. These parameters may be sufficient to activate pre-existing micro-cracks and to lead to material damage or fracture.

Four different theoretical approaches were proposed to characterize the thermal shock resistance. The first theoretical description of thermal shock was proposed by Kingery [16]. He used a thermo-elastic analysis to define the critical temperature difference initiating fracture. This approach is focused on the conditions that control the fracture nucleation.

Another approach was proposed by Hasselman [17] who treats the crack propagation rather than the crack nucleation. His theory enables to characterize the critical temperature difference as well as the damage state of the material. Hasselman takes into consideration the pre-existing cracks instability in relation with the temperature difference.

A statistical approach proposed by Manson [18] is based on Weibull model applied to the case of thermal shock. He showed that the surface stress intensity is higher than the expected values for high probability of fracture. A more realistic approach known as the local approach in comparison with the preceding global approaches was proposed by Evans [19] and completed by Schneider [20]. This model gives numerically some new possibilities and a more precise description of the thermal shock. It is based on a thermo-elastic analysis by integrating the material defaults size to quantify the damage. This fine analysis enables to treat the processes occurring during the thermal shock. It takes into account the transitory character of the thermal shock by determining at every instant the transient temperature profile, the corresponding transient stress state and the stress intensity factor in relation with the crack size.

Experimental methods used for controlling thermal shock damage are numerous [21–23]. There are static methods for measuring the material damage: the weight loss and the mechanical strength deterioration. Other dynamic methods allow controlling the damage by measuring the frequency disturbances and the stationary or moving waves damping caused by the thermal shock [21]. Many researchers have worked on the indentation technique with different cooling means, there are those who use water [24–26], and others use air [27,28].

The aim of this work is to study the thermal shock resistance (measured by indentation air quenching) of alumina ceramics processed by SPS and Natural Sintering, and to compare the mechanical properties of both types of samples.

2. Experimental procedure

2.1. Sample preparation

The starting material used in this study was a commercial α-alumina nano-powder (Grade: Baikalox-BMA15, Baikowski), with purity 99.99% and average particle size 150 nm. Samples for natural sintering were prepared via slip casting. This last method is chosen for its ability to obtain highly densified samples [29–31]. A quantity of 50 g of BMA15powder was dispersed in 50 g of ionized water to form slurry, a pH=3 (obtained with hydrochloric acid) was established to ensure good electrostatic dispersion. The slurry was then milled during 50 h by ball milling with alumina milling media. Every two hours, the pH was re-adjusted to 3 and the dispersion state was checked by laser particle size analysis (Mastersizer 2000).

Before grinding, the particle size distribution is bi-modal (Fig. 1), agglomerates of several microns were observed. A 50 h milling-time is sufficient to obtain a monomodal particle size distribution centered on150 nm. Samples for Spark Plasma Sintering (SPS) were not shaped before sintering (the powder was simply poured in the SPS die just before sintering).

2.2. Sintering

Two kinds of sintering processes were examined: natural sintering and SPS sintering.

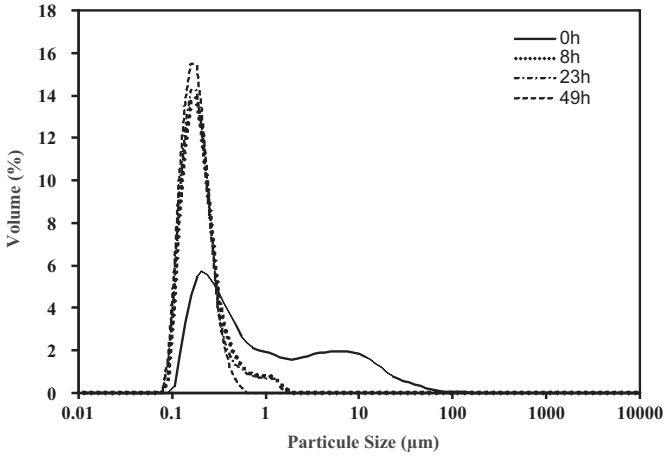

Fig. 1. Effect of grinding time on particle size distribution.

2.2.1. Natural sintering

A degassing of 3 min was performed before casting to remove air bubbles. The slip was cast into plaster molds (with PVC borders) to form plates (50×45 mm^2, 10 mm thick) To avoid the appearance of cracks during drying, a slow drying process is applied: 3 days in 100% humid atmosphere, then 2 days in atmosphere dried with silica gel, then at room atmosphere for 2 days and finally in an oven at 50 °C for 5 days. Finally, the surface layer is removed mechanically to avoid any contamination by the plaster mold.

All green plates were debinded at 600 °C for 1 h (heating ramp: 1 °C/min and cooling ramp: 5 °C min^{-1}) sintered using the following cycle: heating at 1.6 °C min^{-1} up to dwell temperature (1200–1500 °C, every 100 °C) followed by a 1 h or 3 h dwell at this temperature, and natural cooling in the furnace. Bars ($40 \times 4 \times 3$ mm^3) were finally cut from the plates using a diamond saw.

2.2.2. Spark Plasma Sintering

A sintering apparatus (FCT System HPD 25, Germany) was used. Powders (45 g) were loaded into a cylindrical carbon die with an inside diameter of 50 mm. The samples were heated by passing a pulsed current through two electrodes and also through the sample maintained under uniaxial pressure by the electrodes. The sintering cycles were as follows. The temperature reached 450 °C for a period that varies between 3 and 5 min, was then monitored and controlled by an optical pyrometer focused on the surface of the matrix and automatically regulated. The heating rate was 100 °C min^{-1}. The uniaxial pressure (25 or 50 MPa) was applied when the temperature reached 800 °C, and until the end of the holding time. The maximum sintering temperature was varied between 1150 and 1350 °C, spaced 50 °C. The cycle was followed by natural cooling. After this procedure, discs with a diameter 50 mm and thickness 7 mm were obtained. The sintered samples were then machined as chamfered bars; the final dimensions were $40 \times 4 \times 3$ mm^3.

2.3. Thermal shock experiments

The samples for thermal shock experiments were ground and polished down to 1 μm diamond on the two sides (40×4 mm^2) submitted to the air jet during thermal shock. They were indented in the middle of the polished faces with a Vickers indention at a 196 N load, so as to initiate radial cracks parallel to the edges of the samples (Fig. 2). The length of the crack created was of the order of 450 μm.

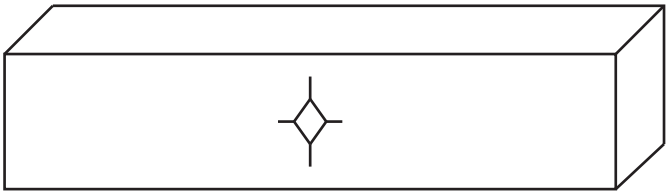

Fig. 2. Radial indentation crack made on the polished face specimen.

The device used for soft thermal shock tests is shown on Fig. 3. The hot part is made of a Pyrox furnace. The thermal shock is applied on hot samples using a compressed air blast under a pressure of 4 bars applied on their two large surfaces. The sample holder allows the transfer between the cold and the hot zones using a pneumatic jack. The other function of the sample holder is the reception of the acoustic activity (piezoelectric sensor) during thermal shock tests. Good characteristics (resistance to thermal shock and fatigue, oxidation resistance and a low thermal conductivity) enable the wave guide to ensure a good coupling between the hot sample and the cold piezoelectric sensor. Ceramic foam is used as an acoustic and thermal insulator between the sample and the sample holder. Two thermocouples allow the measurement of the furnace temperature and that of the sample. A computer enables to record the acoustic activity and control the operations handling.

Thermal shock experiments were conducted between 600 and 900 °C. The samples were heated and maintained in the furnace for 10 min (holding time for homogenization) at the desired temperature. Finally, the samples were rapidly removed from the furnace and the large faces exposed to air jets (two opposite blowers, giving an exchange coefficient h of 600 W m^{-2} K^{-1}) at room temperature. During the exposition to the air jet, the propagation of cracks was followed by acoustical emission, the presence of a peak of acoustical emission being (in this case) related to the unstable propagation of the indentation radial crack. After each test temperature, an evaluation of the radial crack length is made using an optical microscope to better estimate the critical temperature of the thermal shock. If no further cracking is detected, another thermal cycle is applied at higher temperature.

For each kind of samples, 10 specimens were used to determine the critical thermal shock temperature (ΔT_C).

2.4. Characterization

Density is measured by the Archimedes method using deionized water as the immersion medium. Relative densities

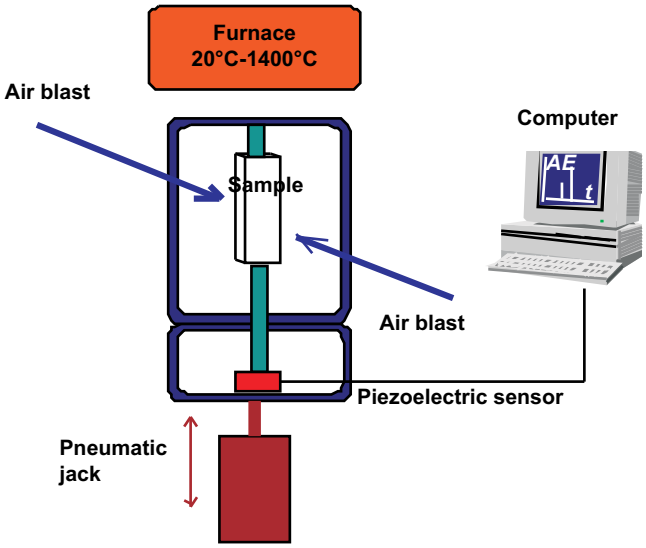

Fig. 3. Schematic apparatus used for soft thermal shock tests (air blast).

between 86% and 99% were measured. Young's modulus was determined before thermal shock by measuring the frequency of externally induced vibration in the samples through the instrument (Grindo-Sonic).

Before the thermal shock test, the samples were tested in four points bending on a universal testing machine. The distances between the outer (L) and inner (L') spans are respectively 35 mm and 10 mm and the used loading rate is of 0.5 mm/min. The fracture stress is given by the following relation (1):

$$\sigma_r = \frac{3F_r(L-L')}{2bw^2} \quad (1)$$

where b is sample width, w is the sample height, F_r is the fracture load, L and L' are the distance between the exterior and interior supports.

The fracture toughness of brittle materials is one of the most important factors which affect the resistance of the materials to thermal shock. K_{I0} values (crack propagation threshold) were measured by indentation technique, using the formula for median radial cracks proposed by Anstis [32](after indentation at a 98 N load with a Vickers diamond). The fracture toughness K_{IC} was measured by rapid fracture of indented four points bending bars (Vickers indentation at 98 N followed by annealing 100 °C below the sintering temperature to relax the residual indentation stresses).

Hardness values were also measured with a Vickers hardness tester (98 N load applied for 10 s).

The following Eq. (2) was used to calculate the critical thermal shock temperature

$$\Delta T_c = \psi^{-1}\frac{(1-\nu)K_{IC}}{E\alpha y a^{1/2}} \quad (2)$$

where E is Young's modulus, α is the coefficient of thermal expansion, $\nu$the Poisson ratio, K_{IC} the fracture toughness, a is the crack length, y is a shape factor of the cracks and ψ is the stress reduction coefficient [28] defined by

$$\psi^{-1} = 1.45 + \frac{4}{\beta} - 0.45\exp\left(\frac{-16}{\beta}\right) \quad (3)$$

where β is function of $h \cdot l/k$, where l is semi dimension (thickness), h the heat transfer coefficient, and k the thermal conductivity.

The values used for the calculations were [28]: $y = 2/\sqrt{\pi}$, $\alpha = 8.1 \times 10^{-6}$ between 20 °C and 1000 °C, $k = 30$ W/m K (20 °C) and $k = 5$ W/m K (1000 °C) and $\nu = 0.3$.

The observations were performed by scanning electron microscopy (SEM; Model Zeiss SUPRA 55 VP). Like mentioned in Ref. [8], measurements of grain size was based on the average linear intercept length of grains in the fracture surfaces taken from 8 to 12 views for each value and confirmed by the Lince software.

Microstructural characterization and Young's modulus measurements were conducted on all samples. However, to get insight on the effect of grain size and sintering technique on the resistance to thermal shock, thermal shock experiments were conducted only on samples with a limited porosity (below 3%), so that the effects of porosity could be considered as negligible.

3. Results and discussion

3.1. Microstructure

Fig. 4 shows SEM micrographs of fractured surfaces of samples sintered by SPS (Fig. 4a) and natural sintering (NS, Fig. 4b). The microstructure of both samples is fine and appears homogeneous. The grain shows more regular shapes with no intra-granular porosity but some pores remained at the grain junctions.

Fig. 5 shows the relative sintered density as a function of sintering temperature for the alumina samples obtained with the two processes (NS and SPS, with a holding time respectively 3 h and 10 min). Generally, it is clear that SPS offers significant advantages over NS for the densification of Al_2O_{3b} nanopowders. In this work, the curves clearly illustrate that Al_2O_3 is fully dense by the natural sintering but SPS process markedly lowers sintering temperature with a short holding time.

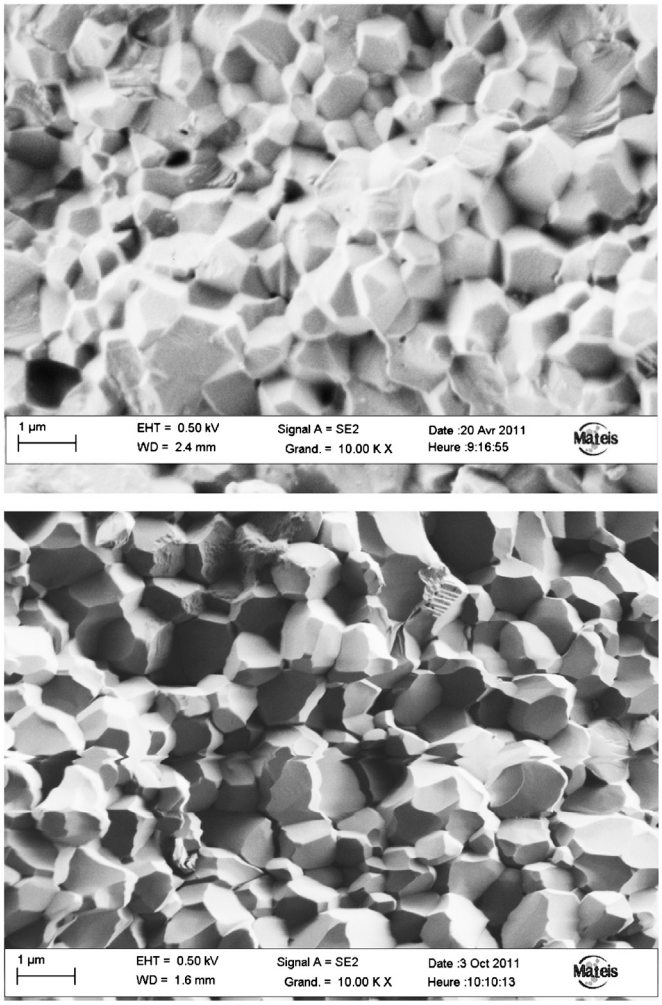

Fig. 4. Fracture surfaces micrographs: (a) natural sintering ($T = 1400$ °C/1 h dwell) and (b) SPS sintering ($T = 1200$ °C/10 min/25Mpa).

In Fig. 6, grain size is plotted versus sintering temperature for samples sintered by the two process routes. We note a similitude between the two curves, with a shifted temperature: similar grain sizes are obtained at temperature interval between 100 °C and 200 °C lower for SPS than for NS. The curves demonstrate that the grain size growth when temperature increases.

Fig. 7 shows the grain size versus relative density for the sintered samples in different conditions. We notice some dispersion for the measured densities. Two domains in the sintering process can be clearly distinguished: at lower sintering temperature, densification takes place without grain growth but when the sintering temperature increases, the grain growth takes place with little densification.

Typically, the sintered ceramic will follow two combined phenomena: both densification and coarsening occur simultaneously. However, to obtain near-theoretical densities, coarsening has to be suppressed until most of the shrinkage has occurred.

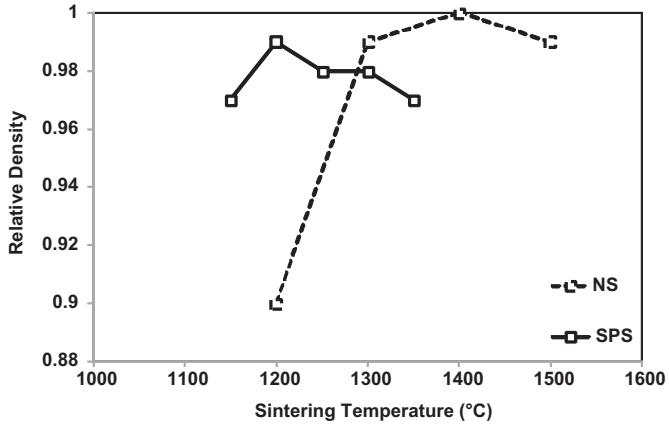

Fig. 5. Relative density versus sintering temperature for the two processes Natural sintering (NS): $t=3$ h and Spark Plasma Sintering (SPS): $t=10$ min, $P=50$ MPa.

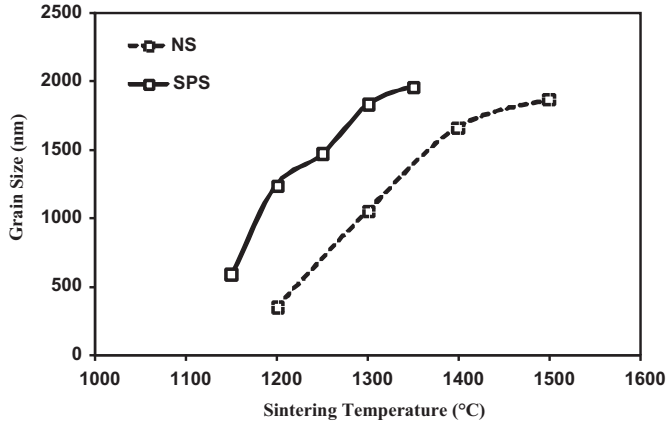

Fig. 6. Evolution of grain size for the specimen, prepared by natural sintering and SPS sintering. Natural sintering (NS): $t=3$ h and Spark Plasma Sintering (SPS): $t=10$ min, $P=50$ MPa.

According to this figure, sintering (NS and SPS) gave a product of high density coupled with small grain size (<2000 nm).

Continuous pores in the initial and intermediate stages of sintering provide a greater drag and hence can inhibit grain growth, more effectively, in comparison to small, isolated pores in the final stage of sintering.

3.2. Mechanical behavior

In this section, we present the effect of microstructure on the mechanical properties of studied alumina.

3.2.1. Elastic modulus

The elastic modulus measured by the dynamic method is represented as a function of porosity (Fig. 8). The shape of the curves (samples obtained by SPS and conventional sintering) seems identical.

The rigidity of the material decreases when the porosity increases. Contrary to the fracture strength, elastic modulus is more sensitive to the closed porosity even if the porosity is low. The elastic modulus decreases by 40% when the porosity is 0.15.

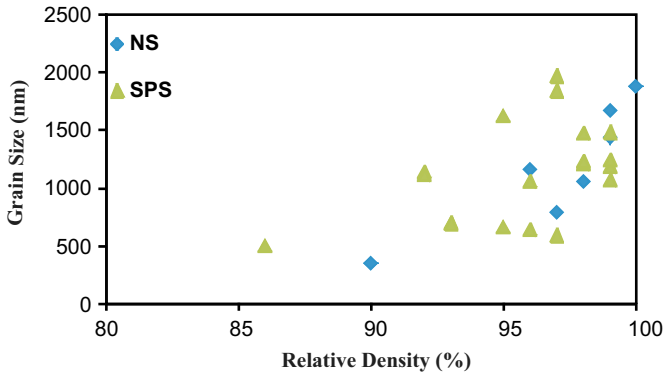

Fig. 7. Grain size versus relative density for all samples (SPS and Natural sintering).

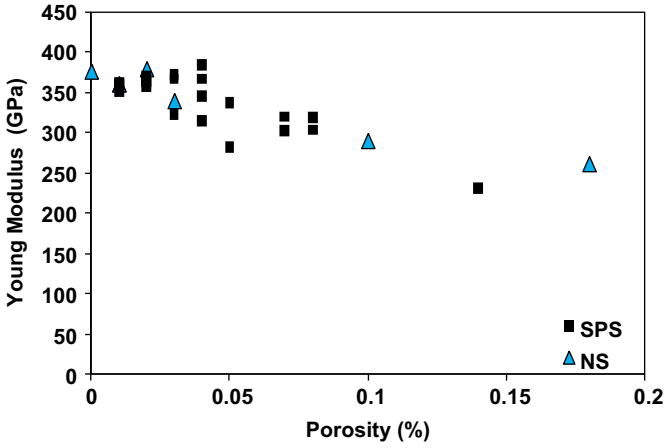

Fig. 8. The evolution of Young's modulus with porosity for the samples obtained by SPS and natural sintering.

3.2.2. Mechanical strength

For the alumina specimens included in this study, Fig. 9 shows the effect of average grain size on the fracture strength. We note that the level of fracture strength was more important for samples sintered conventionally. Moreover, the measured fracture strength increases with the grain size.

Conventional sintering leads to rupture strength between 300 and 600 MPa while the bending strength of sintered samples by SPS does not exceed 400 MPa. It is known that the strength is governed by the most critical defect. In the case of natural sintering, densification was better, through good dispersion of the slip. For conventional sintering NS, prior consolidation, the powder was processed to remove hard agglomerates.

The increase in rupture strength depending on the grain size is due to the fact that the small grain size was obtained at low temperatures. Under these conditions, densification has not yet taken place and the porosity is high, which causes lower mechanical strength. In the case of SPS sintering, densification is lower because the presence of agglomerates (in the nanopowder) leads to a lower strength.

3.2.3. Fracture toughness

The fracture toughness for submicrometer grained Al_2O_3 ceramics were measured by indentation. The average fracture toughness (K_{IC}) was plotted as a function of grain size (Fig. 10). It appears that toughness measured for the NS specimen increases slightly with grain size. In the case of the specimen sintered by SPS, toughness stays constant during grain growth. Fig. 11 shows that in the limited range of porosity used here (below 3%), the sensitivity of K_{IC} to the presence of porosity is not measurable, although theoretically the presence of pores in the ceramic should embrittle it.

3.3. Thermal shock resistance

The samples were submitted to thermal shocks. The detection of an acoustic emission peak is related to the appearance of unstable propagation of the radial crack.

Fig. 12. shows an example of acoustic emission recorded during the thermal shock (6 s) for a critical temperature difference (ΔT_c=792 °C and ΔT_c=724 °C respectively for

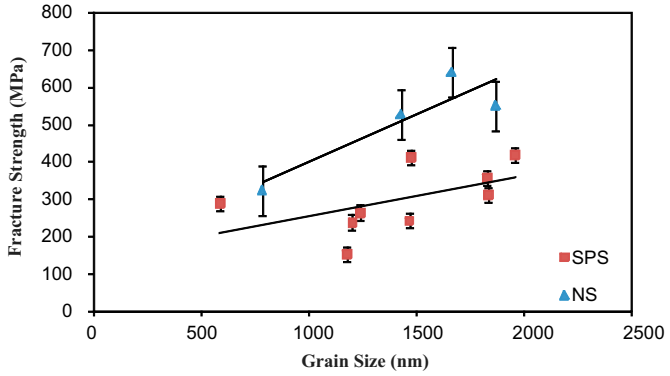

Fig. 9. Effect of grain size on the mechanical strength measured for the two types of specimen.

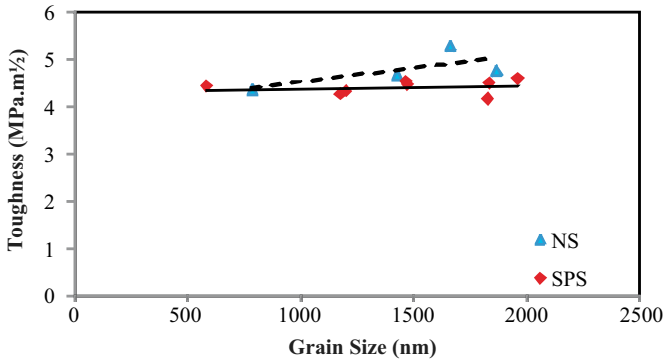

Fig. 10. Fracture toughness versus grain size for sintered sub-micrometer alumina by the two methods (SPS and conventional).

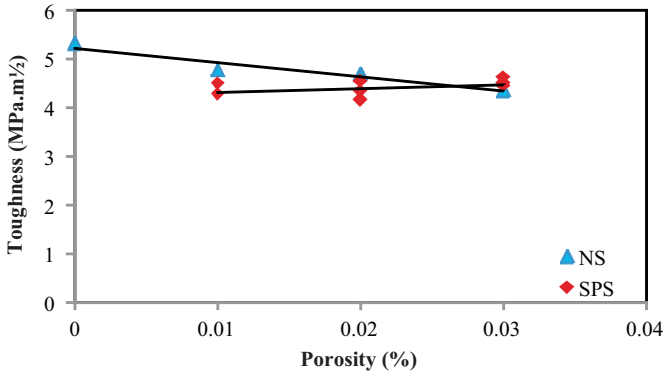

Fig. 11. Fracture toughness versus porosity for the sintered alumina (two routes).

NS and SPS samples). One acoustic event is observed that corresponds to the propagation of a radial indentation crack in the longitudinal direction. It clearly appears that acoustic activities took place 4 s after the cooling began. At this moment, the transient stress gradient state through the samples thickness is maximal.

When the temperature difference is large, the generated stresses become more important leading therefore to a precocious early cracking occurring at the beginning of the cooling process. A relation exists between the initial thermal shock temperature and the acoustic activity.

We remind that the samples tested during the thermal shock were polished and indented at the center of the large surface onto which air is directed. A small scattering of the radial cracks length was observed. These artificial defects have a direct influence on the values of the tensile strength and the critical temperature difference.

Low fracture strength was caused by large artificial defects. During the thermal shock, transient thermal stress propagates this critical radial crack. When the mechanical strength increases, the thermal shock resistance (critical temperature difference) increases (Fig. 13).

Fig. 14 shows that the critical thermal shock temperature seems to decrease with porosity. However, given the scattering of the data this evolution is not significant. Moreover, since the porosity of our samples is very low, so it does not affect

thermal shock behavior. An influence of pore size could not be recognized.

Fig. 15 represents the evolution of the critical temperature as a function of grain size. We note that, despite a large scattering, ΔT_C increases together with the grain size. This is coherent with the increases of toughness and strength with grain size shown in Figs. 10 and 11: larger grains (in the range considered here, e.g. upto 2 μm) means stronger and tougher material thus better resistance to thermal shock.

According to Hasselman's theory [17], residual strength and elastic modulus are important parameters to critical thermal shock temperature. Indeed, the critical thermal shock temperature difference significantly varies with the strength over elastic modulus ratio (Fig. 16). The modulus depends on the closed porosity (volume), while the resistance depends on the surface defects. During thermal shock test, surface defects are predominant (so strength prevails).

Fig. 17 shows the critical temperature difference calculated (using Eq. (2)) and measured for the two types of samples (natural sintering and SPS). In this equation, we introduced measured values K_{1c} toughness and elastic modulus E. Expansion coefficients and Poisson are taken constant. The measured values are between 650 °C and 800 °C for all

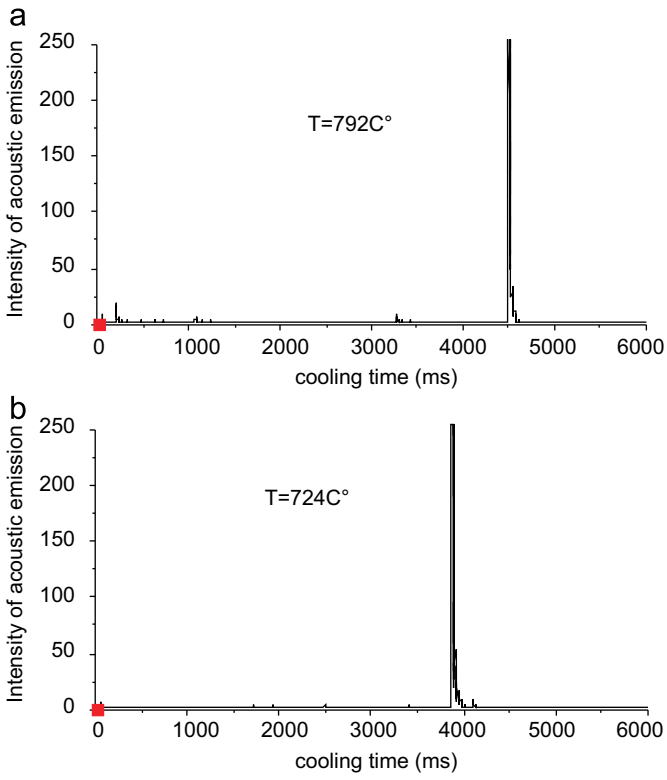

Fig. 12. The critical temperatures for samples;(a) natural sintering and (b) SPS sintering.

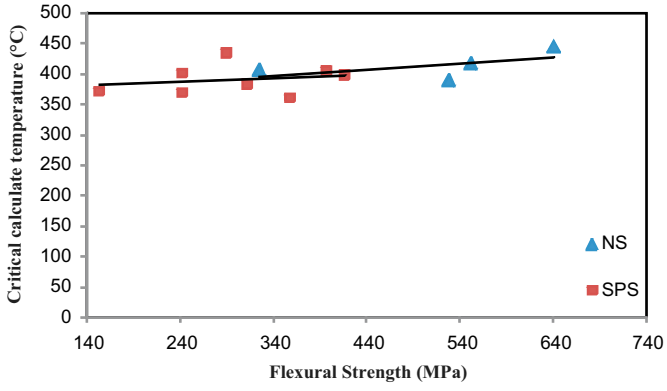

Fig. 13. Critical thermal shock temperature versus retained flexural strength.

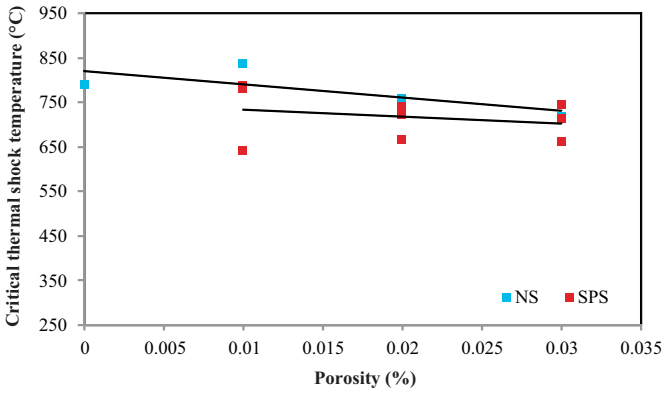

Fig. 14. Critical thermal shock temperature versus specimen porosity.

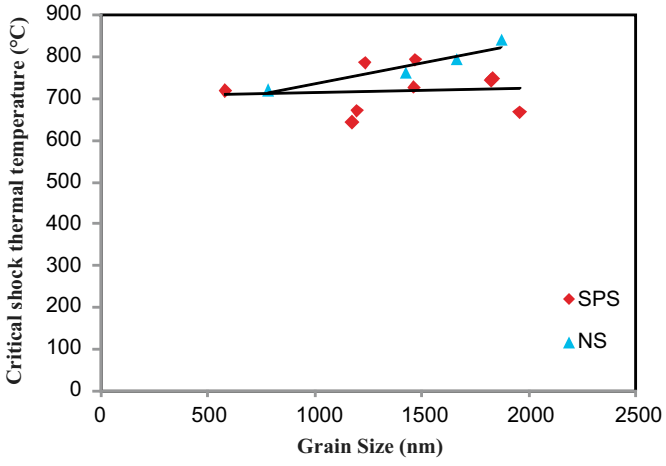

Fig. 15. Critical thermal shock temperature versus grain size.

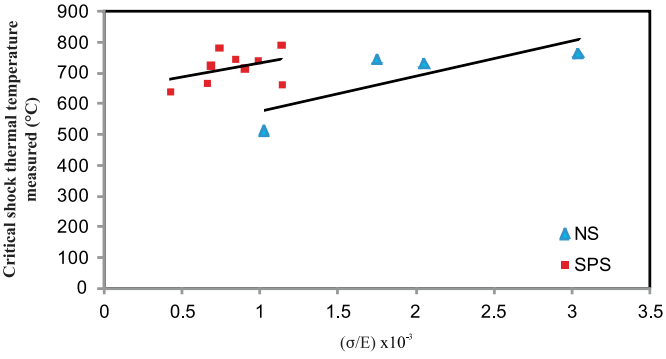

Fig. 16. Critical thermal shock versus fracture strength and elastic modulus.

processing conditions. The calculated values are more sensitive to mechanical strength (greater slope).

We distinguish two areas

Area of low resistance ($\sigma < 300$ MPa): they correspond to the samples sintered by SPS. The fine microstructure leads to low mechanical strength. We recall that the weak mechanical strength was obtained at low sintering temperatures. Similarly, the samples sintered by SPS have low stress at fracture due to the non-disintegration of nanometer powder. Similarly, the critical thermal differences are less important. The experimental results are more important than the calculated ones.

Areas of higher strength ($\sigma > 300$ MPa): we note the calculated critical values are higher. This range corresponds to the sample results obtained by natural sintering. Therefore, they have a larger grain size and a higher porosity. The difference between the measured and calculated values is more significant.

One should keep in mind that the thermal conductivity k has an important influence on the calculated ΔT_C. It was considered constant for the calculation, whereas it really varies with temperature. Moreover, the calculated ΔT_C is directly proportional to the shape factor y, which was chosen equal to $2/\sqrt{\pi}$ by lack of a better estimate while y can vary from 1.1 to 1.5 depending on the crack geometry. Thus the calculated values may not be accurate. Besides, the fracture strengths were measured on a limited number of samples, making their values subject to caution.

4. Conclusion

From an alumina nanopowder and by two different routes (Spark Plasma Sintering and Natural Sintering) we obtained similar structures. Densification of 90–100% and grain size ranging from 500 nm to 2000 nm are observed.

The optimum mechanical properties are obtained for samples most dense for both sintering techniques. The thermal shock resistance (critical temperature difference) depends on the microstructure (porosity and grain size) and therefore on mechanical properties. In the range of grain sizes examined here (below 2 μm), the coarser microstructures present improved mechanical strength and toughness, thus better thermal shock resistance. As the material toughness is more significant as the initiation of cracking due to thermal shock is retarded. Overall, the sintering technique in itself seemed to have no effect on thermal shock resistance: similar microstructures obtained by both SPS and NS present similar resistance to thermal shock.

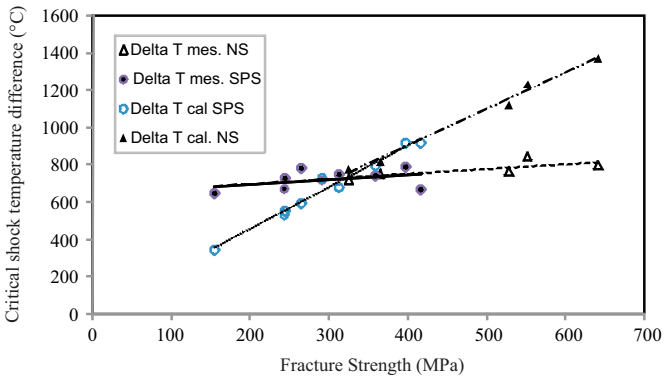

Fig. 17. Critical shock temperature difference measured and calculated versus fracture strength for specimens sintered by natural method and by SPS.

References

[1] C.E. Borsa, N.M.R. Jones, R.I. Todd, Influence of processing on the microstructural development and flexural strength of Al_2O_3/SiC nanocomposites, Journal of the European Ceramic Society 17 (1997) 865–872.
[2] T. Sekine, T. Nakajima, S. Ueda, K. Niihara, Reduction and sintering of a nickel-dispersed-alumina composite and its properties, Journal of the American Ceramic Society 80 (1997) 1139–1148.
[3] P. Bizot, R. Nizard, L. Sedel, Centre Médico-chirurgical de la porte de Pantin Paris in maîtrise orthopédique No 11 Février, Hopital Lariboisière, Paris, 2002.
[4] K. Niihara, A. Nakahira, Structural ceramic nanocomposites by Sintering method: role of nano-size particles, Ceramic Society of Japan (1991) 404–417.
[5] X. Kuang, G. Carotenuto, L. Nicolais, A review of ceramic sintering and suggestions on reducing sintering temperatures, Advanced Performance Materials 4 (1997) 257–274.
[6] R. Chaim, Superfast densification of nanocrystalline oxide powders byspark plasma sintering, Journal of Materials Science 41 (2006) 7862–7871.
[7] G.D. Zhan, J. Kuntz, J. Wan, J. Garay, A.K. Mukherjee, Alumina-based nanocomposites consolidated by spark plasma sintering, Scripta Materialia 47 (2002) 737–741.
[8] Zhijian Shen, Mat Johnson, Zhe Zhan, Mats Nygren, Spark plasma sintering of alumina, Journal of the American Ceramic Society 85 (8) (2002) 1921–1927.
[9] R. Chaim, Superfast densification of nanocrystalline oxide powders by spark plasma sintering, Journal of Materials Science 41 (2006) 7862–7871.
[10] C. Dibyendu, S. Bysakh, K. Muraleedharan, T.N. Rao, R. Sundaresan, Spark plasma sintering of magnesia-doped alumina with high hardness and fracture toughness, Journal of the American Ceramic Society 91 (1) (2008) 203–208.
[11] Dibyendu Chakravarty, G. Sundararajan, Effect of applied stress on IR transmission of spark plasma-sintered alumina, Journal of the American Ceramic Society 93 (4) (2010) 951–953.
[12] M. Hamidouche, N. Bouaouadja, C. Olagnon, G. Fantozzi, Thermal shock behaviour of mullite ceramic, Ceramics International 29 (2003) 599–609.
[13] D.P.H Hasselman, Thermal stress resistance of engineering ceramics, Materials Science and Engineering 71 (1985) 251–264.
[14] Z. Malou, M. Hamidouche, N. Bouaouadja, G. Fantozzi, Statistical analysis of a soda lime glass thermal shock resistance, Ceramics – Silikáty 55 (3) (2011) 215–221.
[15] S. Jurgen, C. Nils, R. Jurgen, Journal of the European Ceramic Society 17 (1997) 727.
[16] W.D. Kingery, Factors affecting thermal stress resistance of ceramic materials, Journal of the American Ceramic Society 38 (1) (1955) 3–15.
[17] D.P.H. Hasselman, Unified theory of thermal shock fracture initiation and crack propagation in brittle ceramics, Journal of the American Ceramic Society 52 (11) (1969) 600–604.
[18] S. Mansons, R.W. Smith, Theory of thermal shock resistance of brittle materials based on Weibull's statistical theory of strength, Journal of the American Ceramic Society 38 (1) (1955) 18–27.
[19] A.G. Evans, Thermal shock fracture in ceramic materials, Proceedings of the British Ceramic Society 25 (1975) 217–235.
[20] G.A. Schneider, Thermal shock criteria for ceramics, Ceramics International 17 (1991) 325–333.

[21] F. Mignard, C. Olagnon, G. Fantozzi, Acoustic emission monitoring of damage evaluation in ceramics submitted to thermal shock, Journal of the European Ceramic Society 15 (1995) 651–653.
[22] M. Hamidouche, N. Bouaouadja, C. Olagnon, G. Fantozzim, Thermal shock behaviour of mullite ceramic, Ceramics International 29 (2003) 599–609.
[23] Z. Malou, M. Hamidouche, N. Bouaouadja, G. Fantozzi, Statistical analysis of a soda lime glass thermal shock resistance, Ceramics – Silikáty 55 (3) (2011) 215–221.
[24] R. Sung Choi, A.Jonathan Salem, Thermal shock behavior of silicon nitride flexure beam specimens with indentation cracks, Journal of the American Ceramic Society 77 (1994) 835.
[25] T. Andersson, D.J. Rowcliffe, Indentation thermal shock test for Ceramics, Journal of the American Ceramic Society 79 (6) (1996) 1509–1514.
[26] B. Legendre, F. Osterstock, On the quatification of quenching transient thermal stresses in brittle solids using Vickers indentations, Journal of Materials Science Letters 156 (1997) 684.
[27] M. Saadaoui, C. Olagnon., G. Fantozzi, Evaluation of short crack *R*-curve behavior of alumina under thermal hock loading, Journal of Materials Science Letters 15 (1996) 64.
[28] F. Hugo, J.C. Glandus, Thermal shock of alumina by compressed air cooling, Journal of the European Ceramic Society 27 (2007) 1919–1925.
[29] F.F. Lange, Powder processing science and technology for increased reliability, Journal of the American Ceramic Society 72 (1989) 3–15.
[30] J. Seidel, N. Claussen, J. Rodel, Reliability of Alumina Ceramics, 2: Effect of Processing, Journal of the European Ceramic Society 17 (1997) 727–733.
[31] J. Ma, L.C. Lim, Effect of particles size distribution on sintering of agglomerate-free submicron alumina powder compacts, Journal of the European Ceramic Society 22 (2002) 2197–2208.
[32] G.R. Anstis, P. Chantikul, B.R. Lawn, D.B. Marshall, A critical evaluation of indentation techniques for measuring fracture toughness by direct crack measurements, Journal of the American Ceramic Society 64 (9) (1981) 533–538.